INTERNATIONAL JOURNAL FOR NUMERICAL METHODS IN FLUIDS
*Int. J. Numer. Meth. Fluids* 2005; **48**:1175–1197
Published online 24 March 2005 in Wiley InterScience (www.interscience.wiley.com). DOI: 10.1002/fld.942

# Comparative study of the continuous phase flow in a cyclone separator using different turbulence models‖

H. Shalaby[1,‡], K. Pachler[2,§], K. Wozniak[3,*,†] and G. Wozniak[1,¶]

[1] *Multiphase Research Group, Technical University of Chemnitz, Chemnitz, Germany*
[2] *AVL LIST GmbH, Hans List Platz 1, A-8020 Graz, Austria*
[3] *SIVUS gGmbH, Schulstr. 38, D-09107 Chemnitz, Germany*

SUMMARY

Numerical calculations were carried out at the apex cone and various axial positions of a gas cyclone separator for industrial applications. Two different NS-solvers (a commercial one (CFX 4.4 ANSYS GmbH, Munich, Germany, *CFX Solver Documentation*, 1998), and a research code (*Post-doctoral Thesis*, Technical University of Chemnitz, Germany, September, 2002)) based on a pressure correction algorithm of the SIMPLE method have been applied to predict the flow behaviour. The flow was assumed as unsteady, incompressible and isothermal. A $k$–$\varepsilon$ turbulence model has been applied first using the commercial code to investigate the gas flow. Due to the nature of cyclone flows, which exhibit highly curved streamlines and anisotropic turbulence, advanced turbulence models such as Reynolds stress model (RSM) and large eddy simulation (LES) have been used as well. The RSM simulation was performed using the commercial package activating the Launder *et al.*'s (*J. Fluid. Mech.* 1975; **68**(3):537–566) approach, while for the LES calculations the research code has been applied utilizing the Smagorinsky model. It was found that the $k$–$\varepsilon$ model cannot predict flow phenomena inside the cyclone properly due to the strong curvature of the streamlines. The RSM results are comparable with LES results in the area of the apex cone plane. However, the application of the LES reveals qualitative agreement with the experimental data, but requires higher computer capacity and longer running times than RSM.

This paper is organized into five sections. The first section consists of an introduction and a summary of previous work. Section 2 deals with turbulence modelling including the governing equations and the three turbulence models used. In Section 3, computational parameters are discussed such as computational grids, boundary conditions and the solution algorithm with respect to the use of MISTRAL/PartFlow-3D. In Section 4, prediction profiles of the gas flow at axial and apex cone positions are presented and discussed. Section 5 summarizes and concludes the paper. Copyright © 2005 John Wiley & Sons, Ltd.

KEY WORDS: cyclone separator; $k$–$\varepsilon$ model; large eddy simulation; RSM

*Correspondence to: K. Wozniak, TU-Chemnitz, Lehrstuhl Strömungsmechanik, Reichenhainerstr. 70, 09126 Chemnitz, Germany.
†E-mail: klaus.wozniak@mb.tu-chemnitz.de
‡E-mail: shhe@imech.tu-chemnitz.de
§E-mail: klaus.pachler@arcor.de
¶E-mail: guenter.wozniak@mb.tu-chemnitz.de

‖Presented in part at the CFX conference, Multiphase Flows in Industrial Applications—Simulation & Experiments. Dresden, Germany, April 2003.

*Received 20 September 2003*
*Revised 19 June 2004*
*Accepted 28 December 2004*

## 1. INTRODUCTION

A cyclone separator is a device, which causes centrifugal separation of materials in a fluid flow. Unlike the slow settling of particles within a settling tank, a cyclone separator system yields fast separation and utilizes less space. Separation occurs quickly because one '$g$' of the gravitational force is replaced by multiple '$g$' of the acting centrifugal force. The material to be separated can consist of solid particles or liquids, i.e. droplets, which are classified according to size, shape, and density. The cyclone utilizes the energy obtained from the fluid pressure gradient to create rotational fluid motion. This rotational motion causes the dispersed phase to separate relatively fast due to the strong acting forces. In widely used reverse flow cyclones of the cylinder on cone design type, Figure 1(a), gases spiral down from a tangential inlet towards the apex of a conical section, where the flow is reversed and the particles are collected in a vessel called hopper. The continuous phase then proceeds upward in an inner core flow towards the gas exit via the outlet tube. Cyclone designs have been developed over many years since their invention. Nowadays, there exists a large number of different types for various industrial applications. Many attempts have been made to improve the performance of

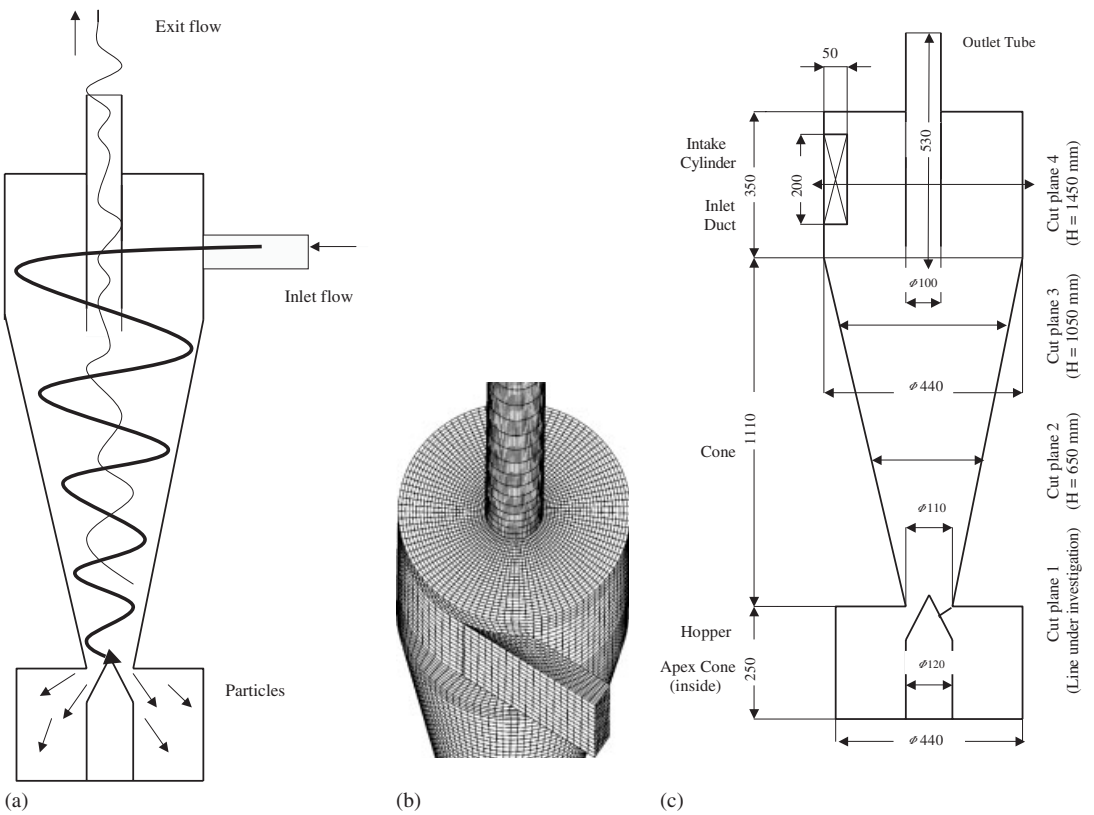


Figure 1. (a) Schematic of the Cyclone Separator Principle; (b) computational grid with 1 300 000 finite volume elements; and (c) location of different cut planes.

 

cyclones by modifying their shape in terms of the ratio of different key dimensions. Normally, the continuous phase flow still carries some particles when it proceeds upward in the inner flow core towards the gas exit. Therefore, a solid apex cone has been incorporated in the cyclone to slow down the flow inside the hopper.

Computational fluid dynamics has become a widely accepted design tool for research and development over the last decade. The number of publications in the field of experimental investigations of cyclone flows is still exceeding by far the number of published numerical investigations. In the past mainly two-dimensional analysis has been performed using radial symmetry of the flow in the cyclone, which sometimes leads to inadmissible simplifications [1]. In recent years much work with three-dimensional predictions of gas-particle flows in cyclone separators has been published. The results show that the quality of the numerical solutions strongly depends on the type of turbulence model used for the continuous phase flow.

Minier and Simonin [2] used a three-dimensional Eulerian–Lagrangian approach on a three-dimensional numerical grid applying a modified $k$–$\varepsilon$ turbulence model. A comparison of the predicted flow field with experimental data was not included in this publication. Furthermore, these authors used a Lagrangian model for the prediction of the particulate phase. Variations of the coefficients of restitution in the particle-wall model from elastic to completely inelastic bouncing behaviour have shown only minor influence on the predicted efficiency grade.

After a number of two-dimensional cyclone flow predictions collected in Reference [3], Boysan *et al.* [4] presented the theory of a three-dimensional modified algebraic Reynolds stress turbulence model (ASM). They found good agreement between the predicted flow field in the investigated cyclone in the range of the so-called potential vortex and an at least qualitative agreement in the core region. The potential vortex appears between the free vortex close to the wall and the forced vortex close to the core.

Gorton-Huelgerth [1] and Staudinger *et al.* [5] performed three-dimensional calculations for a series of standard cyclones using the commercial computer package FLUENT 4.4.7 and FLUENT UNS 4.2.10 [6] with a built-in Reynolds stress turbulence model (RSM). Several different cyclone geometries (e.g. variation of the hopper entrance geometry) have been investigated. Numerical results for the gas velocity field show very good agreement with their laser Doppler anemometer (LDA) measurements.

Frank *et al.* [7], Frank and Wassen [8] and Frank *et al.* [9, 10] developed a three-dimensional Eulerian–Lagrangian approach (MISTRAL/PartFlow-3D) for the numerical prediction of gas-particle flows. Special emphasis has been put on the parallelization of the numerical algorithm for the prediction of the continuous phase. Furthermore, the model is extended for the particle trajectory calculation in order to enable numerical predictions for disperse gas-particle flows in large and complex flow configurations of various industrial applications.

Derksen [11] presented a numerical prediction of a flow in a Stairmand high-efficiency cyclone at $Re = 280\,000$. He performed calculations using a large eddy simulation (LES) based on the Smagorinsky model. His results agree well with experimental data (LDA measurements of the average and RMS values of the tangential and axial velocity).

Souza and Neto [12] have used subgrid scale Smagorinsky modelling to predict the behaviour of a water-fed hydro cyclone. The numerical results captured the main features of the flow pattern and agreed reasonably well with experiments. The authors suggested that LES represents an interesting alternative to classical turbulence models when applied to the numerical solution of fluid flows within hydro cyclones.

 

The objective of the paper is twofold. The first part is devoted to the investigation of the velocity profile at various axial positions and the performance of three different turbulence models: $k$–$\varepsilon$ model, RSM, and LES. Results of these models are compared and discussed also in view of some experimental data published in the literature. The second part focuses on the numerical investigation of the separation area between the cyclone apex cone and the hopper, where to our knowledge, no experimental data exist for.

## 2. TURBULENCE MODELLING

The following section deals with an Eulerian approach for the prediction of three-dimensional gas flows and its application to flow simulation in cyclone separators. The flow is assumed as unsteady, incompressible and isothermal. The momentum balance equations can then be written in conservative form as follows:

$$\frac{\partial K}{\partial t}+\frac{\partial(F-F_v)}{\partial x}+\frac{\partial(G-G_v)}{\partial y}+\frac{\partial(H-H_v)}{\partial z}=0 \tag{1}$$

The inviscid fluxes are

$$K=\begin{pmatrix}\rho\\ \rho u\\ \rho v\\ \rho w\end{pmatrix},\quad F=\begin{pmatrix}\rho u\\ \rho u^2+p\\ \rho vu\\ \rho wu\end{pmatrix},\quad G=\begin{pmatrix}\rho v\\ \rho uv\\ \rho v^2+p\\ \rho wv\end{pmatrix},\quad H=\begin{pmatrix}\rho w\\ \rho uw\\ \rho vw\\ \rho w^2+p\end{pmatrix} \tag{2}$$

Here, $\rho$ is the density, $\mathbf{V}=u\mathbf{i}+v\mathbf{j}+w\boldsymbol{k}$ the velocity vector and $p$ the pressure.

The viscous fluxes are

$$F_v=\begin{pmatrix}0\\ \tau_{xx}\\ \tau_{xy}\\ \tau_{xz}\\ u\tau_{xx}+v\tau_{xy}+w\tau_{xz}\end{pmatrix},\quad G_v=\begin{pmatrix}0\\ \tau_{xy}\\ \tau_{yy}\\ \tau_{yz}\\ u\tau_{xy}+v\tau_{yy}+w\tau_{yz}\end{pmatrix},$$

$$H_v=\begin{pmatrix}0\\ \tau_{xz}\\ \tau_{yz}\\ \tau_{zz}\\ u\tau_{xz}+v\tau_{yz}+w\tau_{zz}\end{pmatrix} \tag{3}$$

 

with the viscous stress tensor

$$\tau_{ij} = \mu \left[ \frac{\partial u_j}{\partial x_i} + \frac{\partial u_i}{\partial x_j} \frac{2}{3} (\nabla \cdot \mathbf{V}) \ \delta_{ij} \right] \tag{4}$$

where $\delta_{ij}$ is the Kronecker delta defined such that $\delta_{ij} = 1$ if $i = j$ and $\delta_{ij} = 0$ otherwise and $\mu$ the molecular viscosity. For incompressible and isothermal flows with constant properties, Equation (1) is reduced to the conservation equations for mass and momentum:

$$\frac{\partial \rho}{\partial t} + \frac{\partial \rho u_i}{\partial x_i} = 0 \tag{5}$$

$$\frac{\partial u_i}{\partial t} + \frac{\partial u_i u_j}{\partial x_j} = -\frac{1}{\rho} \frac{\partial p}{\partial x_i} + \frac{\mu}{\rho} \frac{\partial^2 u_i}{\partial x_j \partial x_j} \tag{6}$$

where $p$ is the pressure. Note, that we use the summation convention. This means that a repeated subscript indicates summation over that subscript.

The $k$–$\varepsilon$ and RSM models were used in the steady-state mode. In order to solve the Reynolds equations it is necessary to apply turbulence models for the Reynolds stresses approximation. CFX-4.4 provides several options of turbulence models, which have been tested and compared: the $k$–$\varepsilon$ model and the Reynolds stress turbulence model of Launder *et al.* [13]. The $k$–$\varepsilon$ model is an eddy–viscosity model that is simple, numerically robust and converging fast. However, those models are known to generate poor results for highly swirling flow as in the case of cyclones where the turbulence is anisotropic. As an alternative, RSM can be used which solves the equations for the individual Reynolds stress components. The RSM model is on the one hand a more fundamental approach to the modelling of turbulence than the eddy–viscosity models but is on the other hand more complex and thus computationally expensive and may cause stability problems. The LES is another approach to predict high Reynolds number flows with high accuracy, however, the requirements on computer resources and the numerical scheme are very high. In LES the large energy-carrying scales are directly computed, and only the effects of the small subgrid scales are modelled.

### *2.1. Standard k–ε turbulence model*

The $k$–$\varepsilon$ turbulence model uses the gradient diffusion hypothesis to relate the Reynolds stresses to the mean velocity gradients and the turbulent viscosity. The turbulent viscosity is modelled as the product of a turbulent velocity and length scale. In the $k$–$\varepsilon$ model the turbulent velocity scale is computed from the turbulent kinetic energy $k$, which is provided from the solution of its transport equation. The turbulent length scale is estimated from the turbulent kinetic energy and its dissipation rate $\varepsilon$. The dissipation rate of the turbulent kinetic energy is provided from the solution of its transport equation.

The $k$–$\varepsilon$ model introduces the two new variables into the system of equations. The momentum equation then reads

$$\frac{\partial \rho u_i}{\partial t} + \frac{\partial \rho u_i u_j}{\partial x_j} = \frac{\partial p'}{\partial x_i} + \frac{\partial}{\partial x_j} \mu_{\text{eff}} \frac{\partial u_i}{\partial x_j} \tag{7}$$

 

where $\mu_{\text{eff}}$ is the effective viscosity accounting for turbulence and $\mu_{\text{t}}$ the turbulent viscosity

$$\mu_{\text{eff}} = \mu + \mu_{\text{t}} \tag{8}$$

$p'$ is the modified pressure given by

$$p' = p + \frac{2}{3}\rho k \tag{9}$$

The $k$–$\varepsilon$ model assumes that the turbulent viscosity is linked to the turbulent kinetic energy and dissipation rate via the relation

$$\mu_t = \rho c_\mu \frac{k^2}{\varepsilon} \tag{10}$$

The values for $k$ and $\varepsilon$ come directly from the differential transport equations for the turbulent kinetic energy and turbulence dissipation rate:

$$\frac{\partial}{\partial x_j}(\rho u k) = \frac{\partial}{\partial x_j}\left[\left(\mu + \frac{\mu_t}{\sigma_k}\right)\frac{\partial k}{\partial x_j}\right] + P_k - \rho\varepsilon \tag{11}$$

$$\frac{\partial}{\partial x_j}(\rho u \varepsilon) = \frac{\partial}{\partial x_j}\left[\frac{\mu_t}{\sigma_\varepsilon}\frac{\partial k}{\partial x_j}\right] + \frac{\varepsilon}{k}(c_{\varepsilon 1}P_k - c_{\varepsilon 2}\rho\varepsilon) \tag{12}$$

The production term has the form

$$P_k = \mu_{\text{t}}\left\{\begin{array}{l} 2\cdot\left[\left(\dfrac{\partial u}{\partial x}\right)^2 + \left(\dfrac{\partial v}{\partial y}\right)^2 + \left(\dfrac{\partial w}{\partial z}\right)^2\right] \\ + \left(\dfrac{\partial u}{\partial y} + \dfrac{\partial v}{\partial x}\right)^2 + \left(\dfrac{\partial u}{\partial z} + \dfrac{\partial w}{\partial x}\right)^2 + \left(\dfrac{\partial w}{\partial y} + \dfrac{\partial v}{\partial z}\right)^2 \end{array}\right\} \tag{13}$$

The constants of the $k$–$\varepsilon$ model are

$$c_\mu = 0.09, \quad c_{\varepsilon 1} = 1.44, \quad c_{\varepsilon 2} = 1.92, \quad \sigma_k = 1.0, \quad \sigma_\varepsilon = 1.3 \tag{14}$$

### 2.2. RSM

The exact transport equation for the Reynolds stress tensor $\overline{u_i u_j}$ is obtained from the momentum equation (5) by multiplying the instantaneous $u_i$ component equation by the fluctuation velocity $u_i'$, adding the two and then time-averaging the result. The result can be written for constant-density flows neglecting body forces after some rearrangement as

$$\underbrace{\frac{D\overline{u_i' u_i'}}{\partial t}}_{C_{ij}} = \underbrace{-\left(\overline{u_i' u_k'}\frac{\partial u_j}{\partial x_k} + \overline{u_j' u_k'}\frac{\partial u_i}{\partial x_k}\right)}_{P_{ij}}$$

 

$$\underbrace{-\frac{\partial}{\partial x_i}\left[\overline{u_i'u_j'u_k'}+\frac{1}{\rho}\left(\overline{p'u_i'}\delta_{ij}+\overline{p'u_j'}\delta_{ik}\right)-\upsilon\frac{\partial\overline{u_i'u_j'}}{\partial x_k}\right]}_{D_{ij}}$$

$$+\underbrace{\frac{p'}{p}\left(\frac{\partial u_i}{\partial x_j}+\frac{\partial u_j}{\partial x_i}\right)}_{\phi_{ij}}-\underbrace{2\upsilon\left(\frac{\partial u_i}{\partial x_k}\frac{\partial u_j}{\partial x_k}\right)}_{\varepsilon_{ij}} \tag{15}$$

Here $P_{ij}$ is the production of $\overline{u_i'u_j'}$; $\varphi_{ij}$ is the pressure–strain term, which promotes isotropy of turbulence; $\varepsilon_{ij}$ is the dissipation (i.e. transformation of mechanical energy into heat in the small-scale turbulence) of $\overline{u_i'u_j'}$; $D_{ij}$ is the convection and diffusion of $\overline{u_i'u_j'}$.

The pressure–strain term, which is an important term since its contribution is significant, is modelled according to Launder *et al.* [13]. The pressure–strain correlation $\varphi_{ij}$ was split into two components that were given as

$$\phi_{ij,1}=-c_1\frac{\varepsilon}{\kappa}\left(\overline{u_iu_j}-\frac{2}{3}\delta_{ij}\kappa\right) \tag{16}$$

$$\phi_{ij,2}=-c_2\left(P_{ij}-\frac{2}{3}\delta_{ij}P_k\right) \tag{17}$$

The constants for $\varphi_{ij}$ are

$$c_1=1.8,\quad c_2=0.6 \tag{18}$$

The comprehensive model includes extra wall reflection terms in the pressure–strain tensor $\varphi$, which are neglected in CFX-4.4. The log-law of the wall was used for the wall treatment following Launder and Spalding [14]:

$$u^+=\frac{1}{\kappa}\ln(y^+)+C \tag{19}$$

where $\kappa=0.41$ is the von Karman constant and $C=5.2$ is a log-layer constant depending on the wall roughness.

### 2.3. LES model

The LES requires the separation of small eddies from large eddies with a filter. For the sake of simplicity, the following section uses one-dimensional notations.

$$\overline{u_i}=\int G(x,x')u_i(x)\,\mathrm{d}x' \tag{20}$$

where $G(x,x')$ is the top-hat filter function. The filter function is large only when $G(x,x')$ is less than the filter width $\Delta_i$, a length scale, over which the averaging is performed. Flow eddies larger than the filter width are defined as 'large eddies' and smaller than the width as

 

'small eddies', i.e.:

$$G(x_i)=\begin{cases} \dfrac{1}{\Delta_i} & |x_i|\leqslant\dfrac{\Delta_i}{2} \\ 0 & |x_i|>\dfrac{\Delta_i}{2} \end{cases} \tag{21}$$

Using the finite volume method, it seems natural to define the filter width, $\Delta_i$, as an average over a grid volume. With the filter, it is possible to derive the governing conservation equations for the momentum (Navier–Stokes) equations, and mass continuity. The filtered Navier–Stokes equations in dimensionless form for an incompressible flow are:

$$\frac{\partial\overline{u_i}}{\partial x_i}=0 \tag{22}$$

$$\frac{\partial\overline{u_i}}{\partial t}+\frac{\partial}{\partial x_j}(\overline{u_i u_j})=-\frac{\partial\overline{p}}{\partial x_i}+\frac{1}{Re}\frac{\partial^2\overline{u_i}}{\partial x_j\partial x_j}-\frac{\partial\tau_{ij}}{\partial x_j} \tag{23}$$

Equations (22)–(23) govern the evolution of the large scales. The effects of the small scales appear in the subgrid-scale stresses,

$$\tau_{ij}=\overline{u_i u_j}-\overline{u_i}\cdot\overline{u_j} \tag{24}$$

which must be modelled. Most of the existing models are of the eddy–viscosity type: they assume proportionality between the anisotropic part of the SGS stress tensor,

$$\tau_{ij}^a=\tau_{ij}-\delta_{ij}\tau_{kk}/3 \tag{25}$$

and the large-scale strain rate tensor, $\overline{S_{ij}}$:

$$\tau_{ij}^a=-2\upsilon_t\overline{S_{ij}}=-\upsilon_t\left(\frac{\partial\overline{u_i}}{\partial x_j}+\frac{\partial\overline{u_j}}{\partial x_i}\right) \tag{26}$$

### *2.4. Smagorinsky model*

The first SGS model was proposed by Smagorinsky [15] in 1963. It is based on the Boussinesq eddy–viscosity approximation that relates the turbulent shear stresses linearly to the strain rates. Equilibrium turbulence and isotropic subgrid scales are assumed. Thus one can write

$$\tau_{ij}=-\upsilon_t S_{ij} \tag{27}$$

where the subgrid viscosity $\upsilon_t$ is defined as

$$\upsilon_t=2(C_s\Delta)^2\sqrt{2S_{ij}S_{ij}} \tag{28}$$

with $C_s=0.1$ being the so-called Smagorinsky constant, for details see Reference [16]. The filter width $\Delta$ was calculated as $\Delta=(\Delta_x\Delta_y\Delta_z)^{1/3}$ according to Reference [16] to account

 

for grid stretching in normal direction. $\Delta_x$, $\Delta_y$ and $\Delta_z$ are the mesh size in the $x$, $y$ and $z$ directions, respectively. The strain rate tensor is given by

$$S_{ij} = \frac{1}{2}\left(\frac{\partial u_i}{\partial x_j} + \frac{\partial u_j}{\partial x_i}\right) \tag{29}$$

The Smagorinsky model depends only on large scales. This means that the model is too dissipative. Therefore the model needs damping in the near-wall region. Otherwise no turbulent phenomenon will develop. A wall damping function has been applied according to Reference [14]

$$f_\mu = 1 - \exp\left[-\left(\frac{y^+}{A^+}\right)^3\right] \tag{30}$$

with $A^+ = 25$ being the so-called *van Driest factor* [17] and $y^+$ a dimensionless wall coordinate defined by

$$y^+ = \frac{u_\tau y}{\upsilon} \tag{31}$$

where $u_\tau$ is the friction velocity, see Reference [15].

## 3. COMPUTATIONAL PARAMETERS

Due to the complex geometry of the cyclone a first guess numerical grid with 80 different grid blocks and about 660 000 finite volume elements had to be designed for first numerical calculations of the continuous phase flow. It will be referred to the first numerical grid as coarse grid. In a second numerical investigation the numerical grid was redesigned using the grid generator ICEM/CFD-HEXA [18] with 80 grid blocks, about 1 300 000 finite volume elements, which will be referred to as fine uniform grid, Figure 1(b). The design of the control volumes was important for several reasons. First of all the control volumes had to be small enough to be able to resolve the significant length scale of the flow. In general this means that a more complex flow with large gradients needs more cells, i.e. a higher cell density in order to capture the correct flow field. More cells will on the other hand lead to a computationally larger problem and require more CPU-time. A compromise is to generate a more dense mesh where large gradients are expected, to increase the mesh size, and to decrease the total number of cells in areas where the flow calculation is less sensitive to the cell size. The mesh size variation has been limited by 1:5 to ensure a smooth solution.

Grid refinement was applied at the gas inlet and to the region in the vicinity of the lower end of the gas exit tube. However, certain restrictions in the mesh generation algorithm of CFX 4.4 prevented an optimal arrangement and design of the finite volume elements in certain regions of the flow geometry. Consequently, strong under relaxation had to be applied for the solution algorithm in order to obtain convergence. This is mainly due to the convergence behaviour of the RSM.

 

### *3.1. Boundary conditions*

Boundary conditions were used at the inlet, which means that the values of the variables are specified. The Reynolds number is about 140 000 at the inlet duct based on the hydraulic diameter and the bulk velocity. At the inlet area, a laminar velocity profile was assumed. In reality, the inlet flow is not laminar ($Re = 140\,000$). However, the results are insensitive to the inlet velocity profile [11]. The variables that have been specified at the inlet were the normal velocity and the turbulence quantities $k$ and $\varepsilon$. The inlet turbulence energy is calculated using

$$k_{\text{inl}} = 1.5(T_u \cdot u_{\text{inl}})^2 \tag{32}$$

and the turbulence dissipation calculated using

$$\varepsilon = \frac{k_{\text{inl}}^{1.5}}{0.3D} \tag{33}$$

$u_{\text{inl}}$ is the mean inlet velocity, $T_u$ the turbulence intensity and $D$ the dissipation length scale at the inlet. $D$ is calculated as $D = 4A/P$, where $A$ is the inlet area and $P$ its perimeter. In case of the RSM the Reynolds stresses must also be specified. By default, the normal stresses are set equal $\frac{3}{2}k_{\text{inl}}$ and the other stresses are set equal to zero.

### *3.2. Solution algorithm MISTRAL PartFlow-3D*

The conservation equations of fluid motion by using LES are solved using the MISTRAL-3D code. The code is based on a finite volume approach, implicit time steps, the SIMPLE [19] algorithm for velocity–pressure coupling, and second-order central-differencing scheme (CDS) for convection. The solution procedure is based on a geometrical multigrid for improved convergence of pressure–velocity coupling on large numerical grids. Computational results presented in this paper have been performed on subclusters of 40 processors of the Chemnitz Linux Cluster CLIC (528 Intel/Pentium III, 800 MHz, 512 Mb RAM per node, $2 \times$ FastEthernet), see Reference [20]. The calculations on the PC clusters were performed with message passing interface (MPI) distribution of LAM-MPI 6.3.5. The CPU-time for the investigation (35 000 time steps) was 242 h. The parallel efficiency achieved was 0.74. On average, five iterations of the SIMPLE algorithm within a time step were performed.

Initially 500 consequently decreasing time steps were performed in order to allow the cyclone flow to reach a fully developed state. The time step reached after the initial iterations was 0.0001 s real (physical) time. This time was kept constant during the rest of the computations. The averaging process was started after the initial iterations and all mean characteristics of the flow have been obtained after averaging over 35.000 time steps. The averaging in the present study was done only with respect to time. The CFL number which defines the relation between the temporal and spatial discretization accuracy was 0.85,

$$\text{CFL} = \Delta t \max_{(x,y,z)} \left( \frac{|\overline{u}|}{\Delta_x} + \frac{|\overline{v}|}{\Delta_y} + \frac{|\overline{w}|}{\Delta_z} \right) \tag{34}$$

Moreover, a second-order accurate implicit time scheme was used in the study.

 

## 4. CONTINUOUS FLOW PREDICTIONS

The investigated cyclone separator is characterized by the geometrical properties shown in Figure 1(c). Comparisons have been made between the calculated and measured axial and tangential velocity profiles at different horizontal cut planes in dimensionless form. The dimensionless velocity profile is scaled with the inlet duct velocity. The experimental data used for validation are published in Reference [21]. The predictions have also been carried out at the apex cone of a cyclone separator. To our knowledge, there is no experimental data material available yet regarding the velocity fields at the apex cone area in the cyclone. Here, the presented comparison is limited between the described three different turbulence models, i.e. $k$–$\varepsilon$, RSM and LES. The location of interest here is the separation area between cyclone apex and hopper. Hence, the velocity profile on a line between the surface of the apex cone and the edge (cut plane 1) of the hopper as shown in Figure 2 has been investigated. The line is normal to the cone surface. The length of the line under investigation is 30 mm in our case. Two of the three velocity components were predicted—the two components in the plane parallel and normal to the apex cone surface. Component 1 ($V_1$) is directed to the tip of the apex cone (axial component), component 2 ($V_2$) has a tangential direction. The velocity profiles were predicted in steps of 90°, see Figure 3.

In Figure 4 the predicted and measured tangential velocity profiles of the continuous phase flow of cut plane 2 are shown. The measured profiles show that the central region in the cyclone rotates like a solid body where the tangential velocity is increasing with an increasing radius. The maximum tangential velocity of approximately 1.24 times the inlet velocity is reached at radius 25% from the centre of the cyclone. Then, the tangential velocity starts to decrease and reaches zero velocity at the wall. Comparison with the experimental data shows, that LES predicts the shape of the tangential velocity profile with higher accuracy when compared to the predictions of the other models. The maximum tangential velocity in case of LES with fine grid is about 1.25 times the inlet velocity at about 25% of the cyclone radius. However, in case of RSM the maximum tangential velocity is about 0.95 times the inlet velocity but is shifted from the centre of the cyclone by about 45% of the cyclone radius. In case of $k$–$\varepsilon$, it is shown that the maximum tangential velocity is about 1.2 times the inlet velocity and shifted toward the wall of the cyclone.

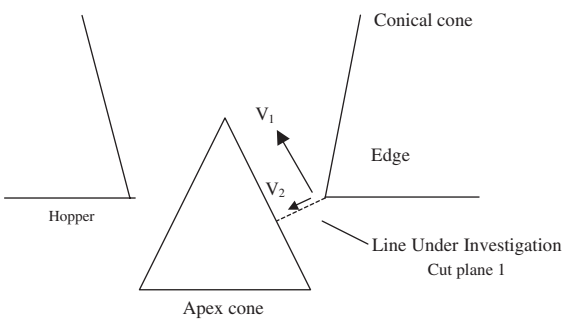


Figure 2. Apex cone frontal view, line under investigation normal to the apex cone surface towards the edge.

 

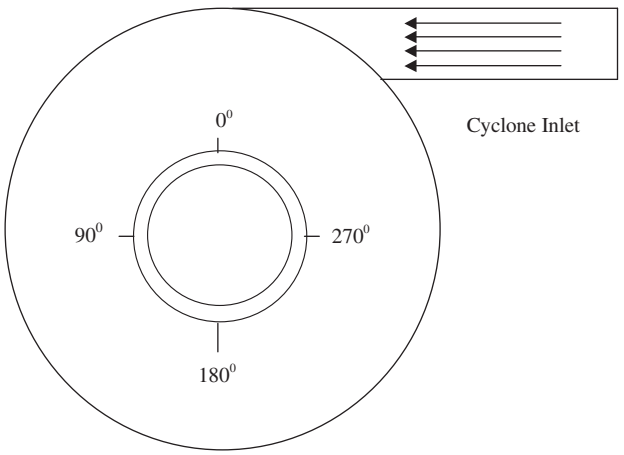


Figure 3. Apex cone top view.

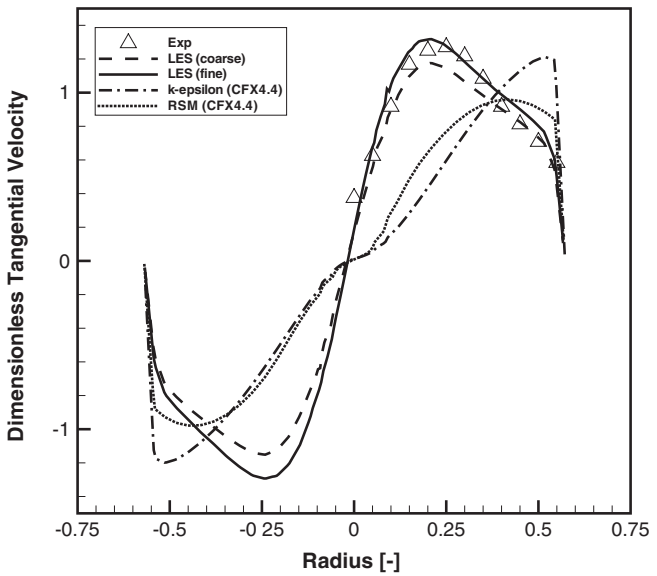


Figure 4. Comparison of three turbulence models and experimental data of Reference [21], tangential velocities at cut plane 2.

In Figure 5 the predicted and measured axial velocity profiles are shown at cut plane 2. Zero on the radial axis characterizes the centre of the cyclone. Positive velocities are directed upward towards the outlet. Both measurements and predictions show the typical axial velocity profiles of a cyclone. There is an outer region close to the wall of the cyclone where the flow is directed downwards. The maximum axial velocities are found in the centre of the cyclone where the flow is directed upwards with 1.1 times the inlet velocity. At about half or more

 

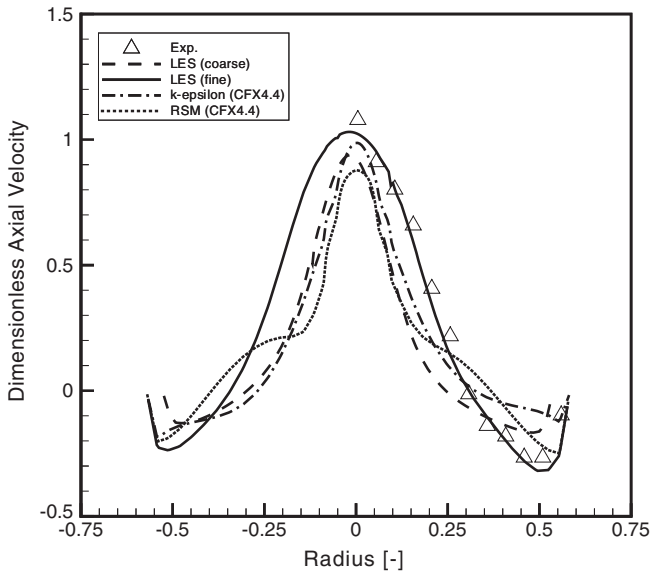


Figure 5. Comparison of three turbulence models and experimental data of Reference [21], axial velocities at cut plane 2.

of the cyclone radius, the flow reverses. The maximum axial velocities are found equal to the inlet velocity in case of LES with fine grid, 0.85 times the inlet velocity in case of RSM, and 0.9 times the inlet velocity in case of $k$–$\varepsilon$. The flow reverses its direction at approximately 35% of the cyclone radius in case of LES, 40% in case of RSM, and 25% in case of $k$–$\varepsilon$. It is also shown here that LES predicts the axial velocity profile more accurate than the RSM and $k$–$\varepsilon$ models as shown in Figure 5 by comparison with the experimental data.

In Figure 6 the predicted and measured tangential velocity profiles are shown for the cyclone at cut plane 3. The same phenomenon of a rotating solid body is predicted especially in case of measurements and LES. It is shown that the LES data obtained with a fine grid compare quite well with the measurement data. The maximum tangential velocity in case of LES is about 1.25 times the inlet velocity at about 25% of the cyclone radius. However, in case of RSM the maximum tangential velocity is about 1.1 times the inlet velocity and shifted from the centre of the cyclone also by about 60% of the cyclone radius. In case of the $k$–$\varepsilon$ model, it turns out that the maximum tangential velocity is about 1.4 times the inlet velocity and the maximum tends to be located close to the wall.

In Figure 7 the predicted and measured axial velocity profiles of cut plane 3 are shown. Also here the positive velocities are directed upward towards the outlet. At this position, it can also be noted that LES with fine grid is most comparable to measurement data at the maximum axial velocity of about 1.2 times the inlet velocity. In case of RSM, the maximum axial velocity is still located at the centre of the cyclone with about 0.65 times the inlet velocity and will then reverse downward at approximately 45% of the cyclone radius. The maximum axial velocity is about 0.7 times the inlet velocity in case of the $k$–$\varepsilon$ model and the flow will also reverse its direction downward at 45% of the cyclone radius.

 

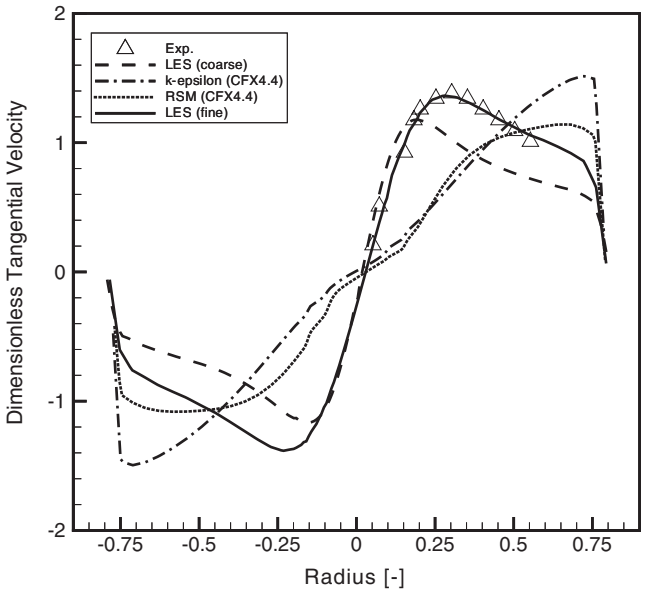


Figure 6. Comparison of three turbulence models and experimental data of Reference [21], tangential velocities at cut plane 3.

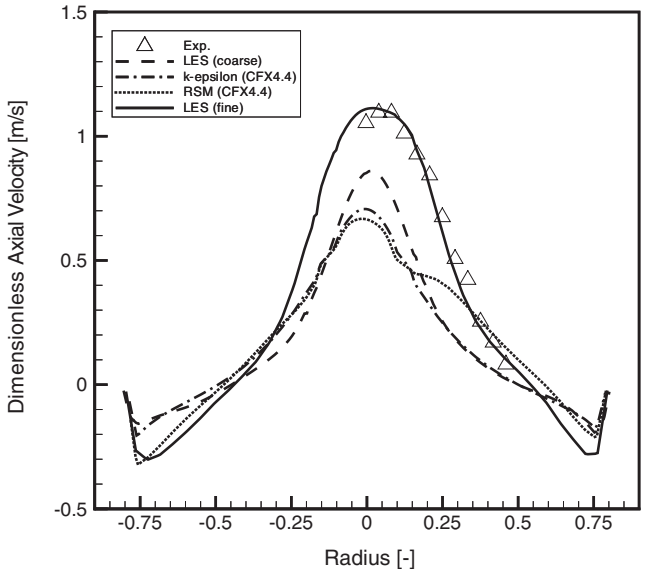


Figure 7. Comparison of three turbulence models and experimental data of Reference [21], axial velocities at cut plane 3.

In Figure 8 the predicted tangential velocity profiles are presented for the cyclone at cut plane 4. It is shown that this plane has two regions; the outlet tube itself and the area outside the tube near the inlet duct. It is noted that outside the outlet tube the maximum tangential

 

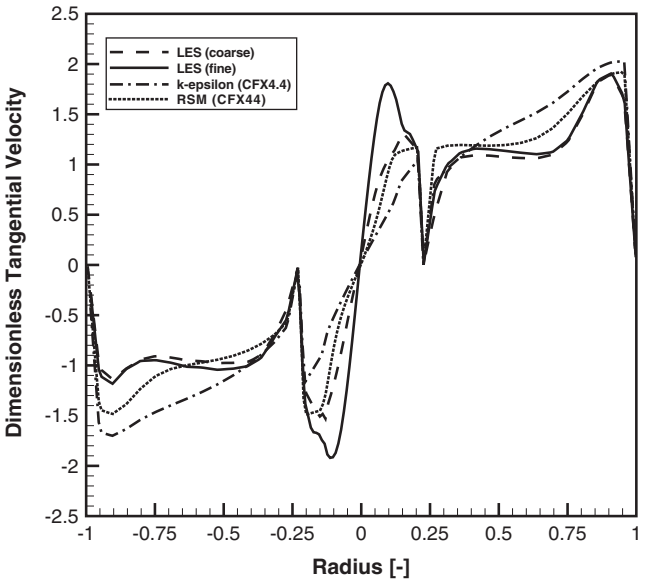


Figure 8. Comparison of three turbulence models, tangential velocities at cut plane 4.

velocity is located with respect to the three turbulence models. The maximum tangential velocity is about 1.9 times the inlet velocity in case of LES, 1.95 times the inlet velocity in case of RSM, and 2 times the inlet velocity in case of the $k$–$\varepsilon$ model. The tangential velocity will tend to zero at the wall of the outlet tube. Inside the outlet tube, the same trend is shown for the maximum tangential velocity shifted from the centre of the tube in case of LES with a maximum velocity of 1.8 times the inlet velocity. However, the maximum velocity in case of RSM is about 1.2 times the inlet velocity and about 0.95 times the inlet velocity in case of the $k$–$\varepsilon$ model. For this (cut plane 4) and the following predictions, no experimental data are available yet.

In Figure 9 the predicted axial cyclone velocity profiles of cut plane 4 are shown. It turns out that the axial velocity outside the outlet tube is slightly below zero. Inside the outlet tube, the maximum axial velocity is about 4 times the inlet velocity in case of LES. However, the maximum velocity in case of RSM is about 2.8 times the inlet velocity and about 2.4 times the inlet velocity in case of the $k$–$\varepsilon$ model.

It should be noted, that the three applied turbulent models are capable to resolve different degrees of flow complexity. The $k$–$\varepsilon$ model predicts as expected a solid body swirl shown in Figures 7 and 8. The flow within the outlet tube is a swirling pipe flow, which can be correctly described only by the LES approach. The reason is the strong anisotropic stress distribution due to the streamlines curvature.

In Figure 10, the predicted tangential velocity profiles at the 0° angle line are shown at the line between the apex cone and the edge of the hopper. The $x$-axis represents the scaled radius of the line under investigation. Zero is attached to the apex cone surface and 1 is attached to the edge of the hopper. Negative tangential velocities are directed downward toward the hopper in case of LES and RSM where the minimum velocity is located at the centre of the line. The minimum tangential velocity is approximately 0.78 times the inlet velocity in case

 

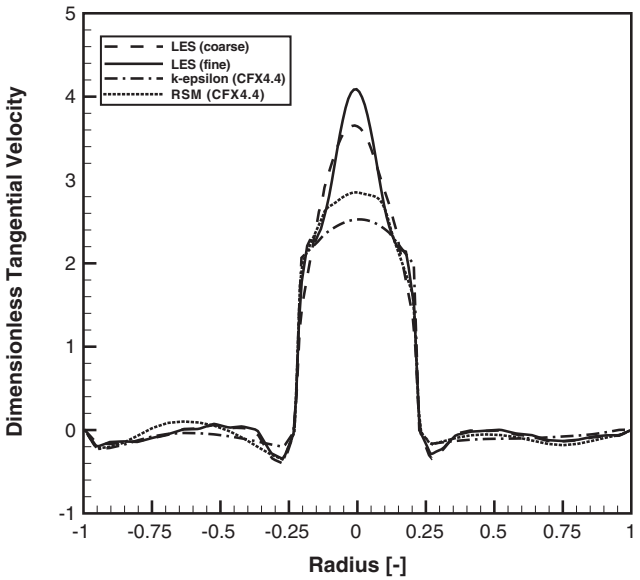


Figure 9. Comparison of three turbulence models, axial velocities at cut plane 4.

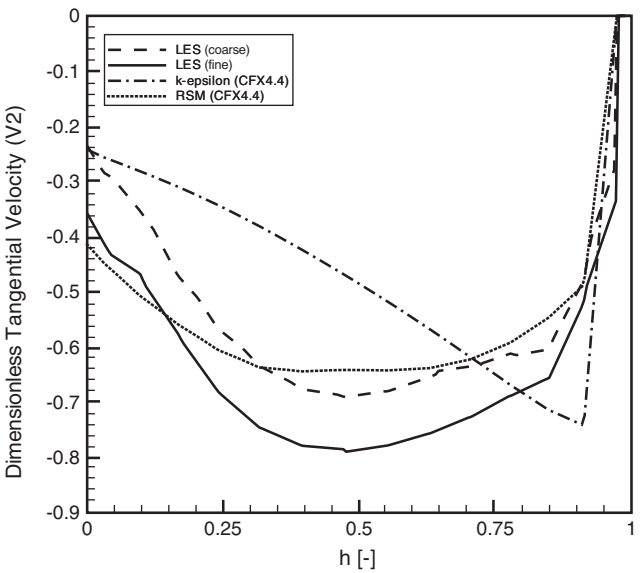


Figure 10. Comparison of three turbulence models, tangential velocities at cut plane 1 at 0°.

of LES and 0.6 times the inlet velocity in case of the RSM model. The flow will tend to slow down close to the surface of the apex cone, which is the reason for incorporating the apex cone. It should be noted, that there is qualitative agreement between LES and RSM data here. However, there is a large deviation in case of the $k$–$\varepsilon$ model.

 

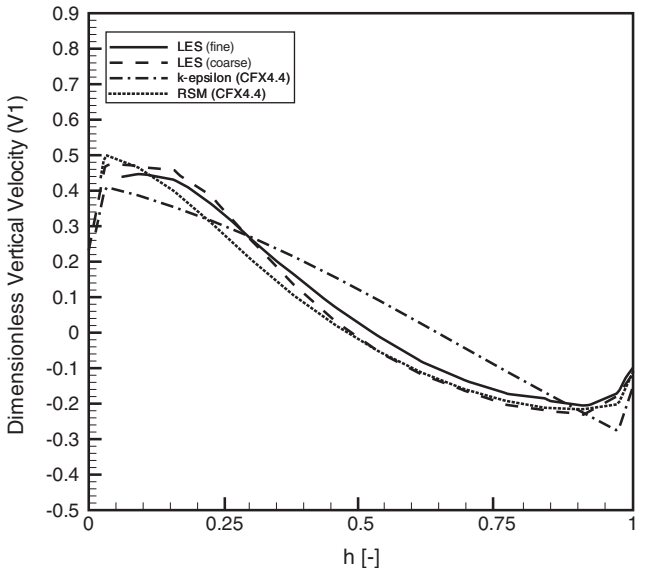


Figure 11. Comparison of three turbulence models, vertical velocities at cut plane 1 at 0°.

In Figure 11, the predicted axial velocity profiles at the 0° angle line are shown. There are outer regions close to the wall of the surface of the apex cone where the flow is directed upwards and close to the edge of the hopper where this flow in turn is directed downward. The maximum axial velocity in case of LES is about 0.48 times the inlet velocity close to the surface of the apex cone and 0.5 times the inlet velocity in case of the RSM. It was also found that there is an agreement between LES and RSM results compared to the $k$–$\varepsilon$ results.

In Figure 12, the predicted tangential velocity profiles at the 180° angle line are shown. Positive velocities are directed upward to the cyclone body in case of the LES and RSM models. The maximum tangential velocity at centre of the line under investigation is about 0.74 times the inlet velocity in case of LES and 0.62 times the inlet velocity in case of RSM models. It should also be noted that there is agreement between LES and RSM, however, there is a large deviation when compared to the $k$–$\varepsilon$ model results.

In Figure 13 representing a 180° angle line, the predicted axial velocity profiles are shown. There are outer regions close to the wall of the surface of the apex cone where the flow is directed downwards and close to the edge of the hopper where the flow is directed upward. The maximum axial velocity in case of LES is about 0.4 times the inlet velocity close to the surface of the apex cone and 0.52 times the inlet velocity in case of the RSM model.

In Figure 14 representing a 90° angle line, the predicted tangential velocity profiles are shown. It can be noted that the maximum tangential velocity is about 0.02 times the inlet velocity in case of LES and RSM at about 60% of the line directed upwards. The flow velocity close to the surface of the apex cone is directed downward with about 0.34 times the inlet velocity in case of LES and 0.3 times the inlet velocity with RSM. In case of $k$–$\varepsilon$, there is a large deviation between the results where the maximum tangential velocity tends to be close to the wall.

 

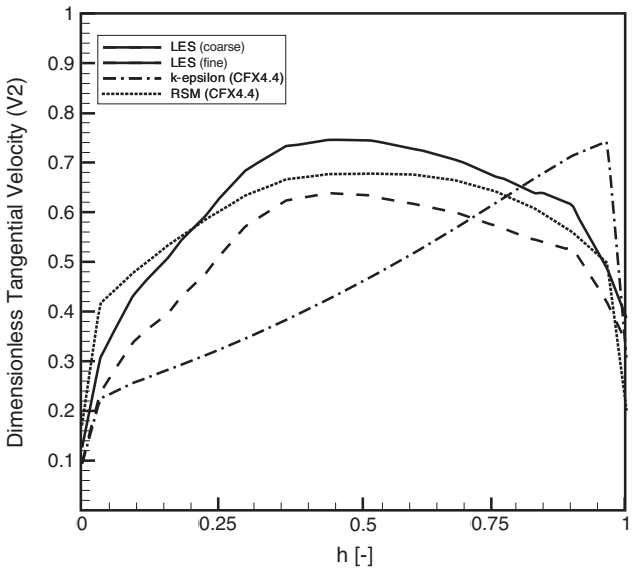


Figure 12. Comparison of three turbulence models, tangential velocities at cut plane 1 at 180°.

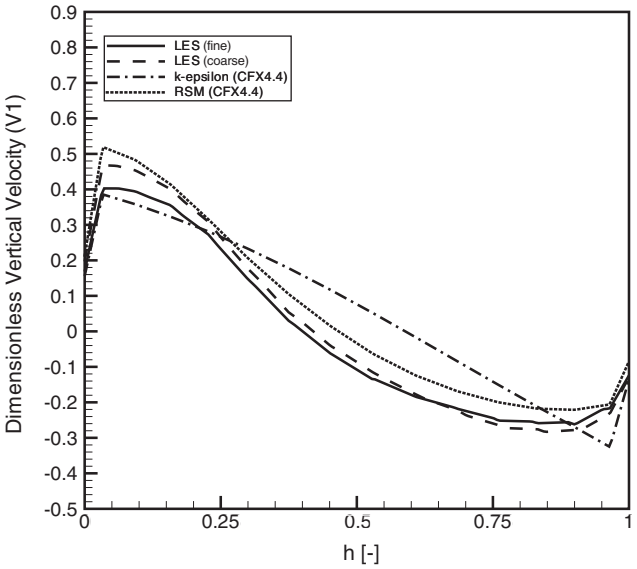


Figure 13. Comparison of three turbulence models, vertical velocities at cut plane 1 at 180°.

In Figure 15 representing a 90° angle line, the predicted axial velocity profiles are shown. The maximum axial velocity in case of LES is about 0.4 times the inlet velocity at about 5% of the line directed upward close to the surface of the apex cone and about 0.33 times

 

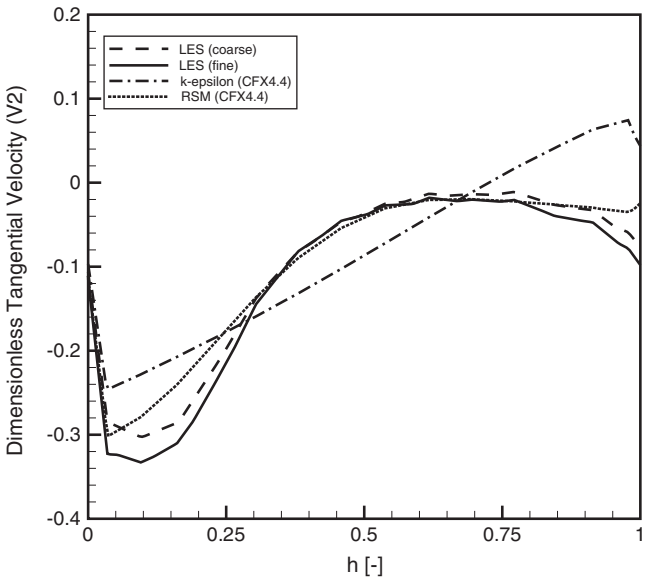


Figure 14. Comparison of three turbulence models, tangential velocities at cut plane 1 at 90°.

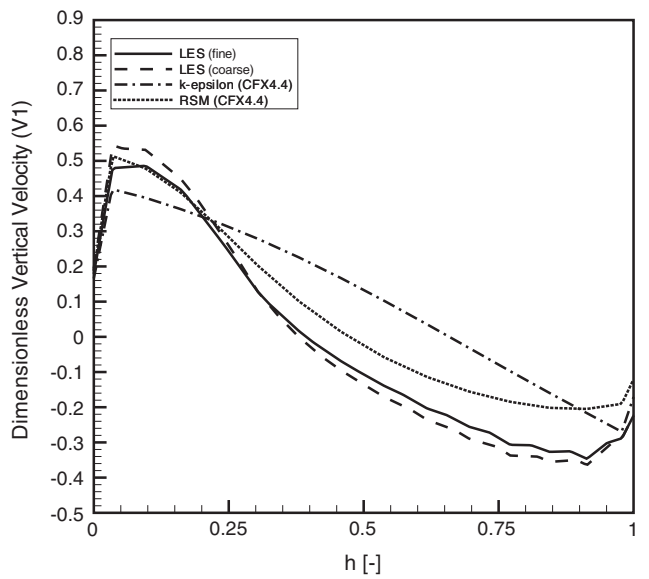


Figure 15. Comparison of three turbulence models, vertical velocities at cut plane 1 at 90°.

the inlet velocity at about 90% of the line directed downward close to edge of the hopper. In case of RSM the maximum axial velocity tends to be close to the surface of the apex cone at the edge of the hopper with about 0.5 times the inlet velocity directed upwards and

 

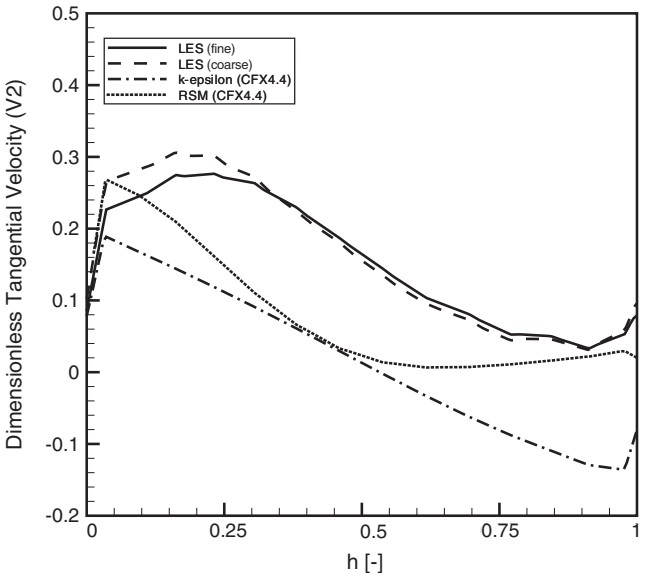


Figure 16. Comparison of three turbulence models, tangential velocities at cut plane 1 at 270°.

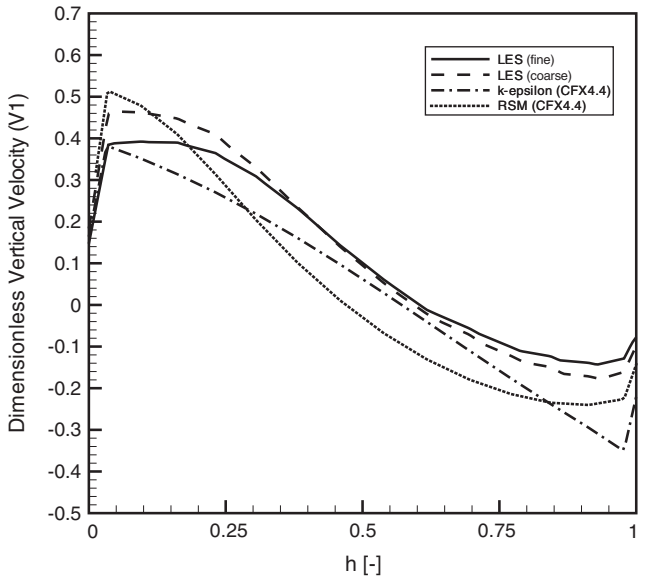


Figure 17. Comparison of three turbulence models, vertical velocities at cut plane 1 at 270°.

0.36 directed downwards, respectively. In case of $k$–$\varepsilon$ the maximum axial velocity tends to be close to the surface of the apex cone at the edge of the hopper with about 0.36 times the inlet velocity directed upwards and 0.18 directed downwards, respectively.

 

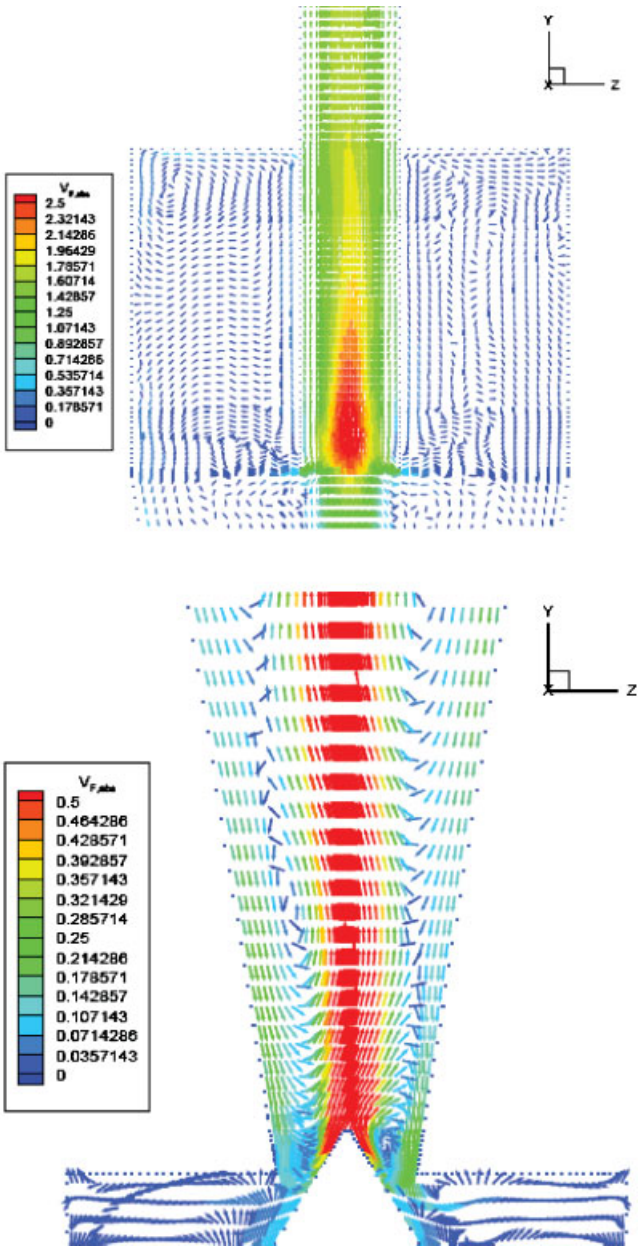


Figure 18. Flow field in the upper and lower part of the cyclone (vertical mid-plane cut).

In Figure 16 representing a 270° angle line, the predicted tangential velocity profiles are shown. It can be noted that LES and RSM are not comparable in this plane. The maximum tangential velocity in case of LES is about 0.26 times the inlet velocity directed upwards at 25% of the line. In case of RSM the maximum tangential velocity is about 0.26 times the

 

inlet velocity directed upwards close to the wall of the apex cone. The minimum tangential velocity in case of RSM is about 0.02 times the inlet velocity directed downwards at the centre of the line. It can also be noted that there is a bigger difference between LES, RSM and $k$–$\varepsilon$ results. However, the maximum tangential velocity tends to be close to the walls.

In Figure 17 representing a 270° angle line, predicted axial velocity profiles are shown. The maximum axial velocity in case of LES and RSM is approximately 0.38 and 0.5 times the inlet velocity and located close to the surface of the apex cone. In case of $k$–$\varepsilon$ the maximum velocity tends to be close to the walls with values of about 0.38 times the inlet velocity.

Finally, the flow field visualized in Figure 18 was gained by LES computations only. It is shown in the upper part of the figure, that recirculating flow appears along the wall of the cylindrical part of the cyclone. Furthermore, it can be observed, that the flow is directed downwards along the outer wall of the outlet tube. In the lower part of Figure 18, a strong secondary flow along conical walls of the cyclone is directed downwards to the hopper. Furthermore, it can be noted that a certain amount of gas flow is entering the hopper. The gas flow is then recirculating along the surface of the apex cone back into the main cyclone body.

## 5. CONCLUSIONS

The nature of the gas flow of a particle cyclone separator is highly swirling with anisotropic turbulence. Therefore, advanced turbulence models such as RSM and LES have to be applied to predict the gas flow behaviour rather than the $k$–$\varepsilon$ turbulence model. Our calculations confirm, that in case of cyclone continuous phase flows the $k$–$\varepsilon$ model generates weak results. The reason for the poor performance of the $k$–$\varepsilon$ model is that the important assumption of isotropic turbulence does not hold in flows with non-uniform pressure distributions such as swirling flows.

The predicted data from the RSM investigations were not as representative as the LES data. The tangential velocity profiles showed that with RSM we tend to obtain a solid body rotation, which reached too far towards the external wall. RSM calculations using a central advection scheme for the momentum equations should be used in future investigations rather than the higher order QUICK scheme. Also, the linear approach for the pressure–strain term in the LRR model seems to be inadequate for such swirling flows.

The results of LES in case of the complex flow in a cyclone compare well with the measurement data found in the literature even when using a coarse grid. This is one key result of our investigations. Therefore, the LES results are very encouraging and have shown that this model is a better alternative to conventional turbulence modelling of cyclone separators. The dynamic behaviour of the flow has been captured, providing important information on the flow structure within the cyclone. Our future objective is to generate further experimental laboratory data especially at the apex cone area in order to validate the presented numerical results and to conduct new investigations, which include the prediction of the disperse-phase behaviour.

## REFERENCES

1. Gorton-Huelgerth A. *Messung und Berechnung der Geschwindigkeitsfelder und Partikelbahn im Gaszyklon*, Reihe 7, Nr. 375. VDI-Fortschritt-Bericht: 1999.
2. Minier J, Simonin O. A numerical approach of cyclone separators. *Proceedings of the 2nd European SYMP, Separation of Particles from Gases*, Nürnberg BRD, March 1992; 121–136.

 

3. Boysan F. *Zyklone zur Abscheidung von Feststoffen aus Gasen*. VDI-Gesellschaft Verfahrenstechnik und Chemieingenieurwesen (GVC), 8. Auflage. Springer: Berlin, 1997; 1–11.
4. Boysan F, Swithenbank J, Ayers WH. Mathematical modelling of gas-particle flows in cyclone separators. *Encyclopedia of Fluid Mechanics*, vol. 4. Solids and Gas-Solids Flows. Gulf Publishing Company: Houston, TX, 1986 (Chapter 42).
5. Staudinger G, Obermaier S, Meisel C. *Treffsicherheit und Zuverlässigkeit der heutigen Zyklonberechnung*, VDI-Bericht 1511. VDI-Verlag: Düsseldorf, 1999; 1–23.
6. Fluent GmbH. *Fluent User Guide Documentation*, 1997.
7. Frank T, Wassen E, Yu Q. A 3-dimensional Lagrangian solver for disperse multiphase flows on arbitary, geometricaly complex flow domains using block structured numerical grids. *Proceedings of the 7th International Symposium on Gas-Particle Flows*, ASME Fluid Engineering Division Summer Meeting, Vancouver, BC, Canada, June 22–26, 1997.
8. Frank T, Wassen E. Parallel efficiency of PVM- and MPI-implementations of two algorithms for the Lagrangian prediction of disperse multiphase flows. *JSME Centennial Grand Congress 1997*, *ISAC '97 Conference on Advanced Computing on Multiphase Flow*, Tokyo, Japan, July 18–19, 1997.
9. Frank T, Wassen E, Yu Q. Lagrangian prediction of disperse gas-particle flow in cyclone separators. *ICMF '98—3rd International Conference on Multiphase Flow*, Lyon, France, June 8–12, 1998. CD-ROM Proceedings, Paper No. 217, 1998; 1–8.
10. Frank T, Schneider J, Yu Q, Wassen E. Experimental and numerical investigation of particle separation in a symmetrical double cyclone separator. *8th International Symposium on Gas-Particle Flows*, ASME Fluids Engineering Division Summer Meeting, San Francisco, CA, USA, July 18–22, 1999. CD-ROM Proceedings, Paper No. FEDSM99-7865, 1999; 1–10.
11. Derksen J. LES-based separation performance predictions of a stairmand cyclone. *10th Workshop on Two-Phase Flow Predictions*, Martin-Luther-Universität Halle-Wittenberg, Halle (Saale), Germany, 9–12 April 2002; 217–226.
12. Souza F, Neto A. Large eddy simulations of a hydrocyclone. *Proceedings of FEDSM ASME Fluid Engineering Division Summer Meeting*, Montreal, Quebec, Canada, 14–18 July 2002; 1–6.
13. Launder B, Reece G, Rodi W. Progress in the development of a Reynolds-stress turbulence closure. *Journal of Fluid Mechanics* 1975; **68**(3):537–566.
14. Launder B, Spalding DB. The numerical computation of turbulent flows. *Computer Methods in Applied Mechanics and Engineering* 1974; **3**:269–289.
15. Smagorinsky J. General circulation experiment with the primitive equations. *Monthly Weather Review* 1963; **91**:99–164.
16. Denev J, Frank T, Pachler K. Large eddy simulation (LES) of turbulent square channel flow using a PC-cluster architecture. *Proceedings of the 4th International Conference on Large-scale Scientific Computations*, Sozopol, Bulgaria, June 4–8, 2003; 1–11.
17. Van Driest ER. On the turbulent flow over a wall. *Journal of Aeronautical Science* 1965; **23**:1007–1011.
18. ICEM CFD Engineering GmbH. *ICEM/CFD Hexa Manual Documentation*, September 1998.
19. Patankar SV. *Numerical Heat Transfer and Fluid Flow*. McGraw-Hill: New York, 1980.
20. Website of the Chemnitz Linux Cluster (CLIC), Chemnitz University of Technology, Germany, http://www.tu-chemnitz.de/urz/anwendungen/CLIC
21. Fraser SM, Abdel Rasek AM, Abdullah MZ. Computational and experimental investigation in a cyclone dust separator. *Proceedings of the Institution of Mechanical Engineers* 1997; **211**(Part E):247–257.

 